


Absence of Walker Breakdown in the Dynamics of Chiral Néel Domain Walls Driven by In-Plane Strain Gradients

Mouad Fattouhi¹,* Felipe Garcia-Sanchez¹, Rocio Yanes¹, Victor Raposo¹, Eduardo Martinez¹, and Luis Lopez-Diaz¹

Departamento de Física Aplicada, Universidad de Salamanca, Salamanca 37008, Spain

 (Received 11 March 2022; revised 13 July 2022; accepted 14 September 2022; published 10 October 2022)

The influence of mechanical strain on the static and dynamic properties of chiral domain walls (DWs) in perpendicularly magnetized strips is investigated using micromagnetic simulations and a one-dimensional model. While a uniform strain allows one to reversibly switch the domain-wall configuration at rest between Bloch and Néel patterns, strain gradients are suggested as an energy-sustainable means to drive domain-wall motion without the need for magnetic fields or electrical currents. It is shown that an in-plane strain gradient creates a force on a domain wall that drives it towards a region of higher tensile (compressive) strain for materials with positive (negative) magnetostriction. Moreover, due to the dependence of the domain-wall internal energy on the in-plane strain, a damping torque proportional to the local strain arises during motion that opposes the precessional torque due to the driving force, which is proportional to the strain gradient. After a transient period, where both the internal DW angle and the velocity change non-monotonically, reaching their maximum values asynchronously, the two torques balance each other. This compensation prevents the onset of turbulent domain-wall dynamics, and steady domain-wall motion with a constant velocity is asymptotically reached for an arbitrarily large strain gradient. Despite this complex dynamics, our work shows that average domain-wall velocities in the range of 500 m/s can be obtained using voltage-induced strain in piezoelectric/ferromagnetic devices under realistic conditions.

DOI: [10.1103/PhysRevApplied.18.044023](https://doi.org/10.1103/PhysRevApplied.18.044023)

I. INTRODUCTION

Reliable, fast, and efficient domain-wall (DW) motion in perpendicularly magnetized media is a key aspect of the development of new spintronic devices for a variety of applications, such as memory [1], sensing [2], logic [3,4], and neuromorphic computing [5,6]. It is well known that when driven by an external force such as an out-of-plane field, a DW changes its internal structure due to the precessional component of the driving force, which rotates it away from its orientation at rest [7]. For low values of the driving force, a terminal DW angle is reached, at which this precessional torque is counterbalanced by a restoring torque that tries to bring it back to its equilibrium orientation, leading to the DW moving rigidly at a constant velocity. Above a certain threshold value, however, this balance is no longer possible, and continuous internal precession of the DW takes place during its motion, with a consequent reduction in speed. This so-called Walker breakdown (WB) [8] is quite a general phenomenon and is present, for example, when the driving force is an out-of-plane field [9] or a spin-polarized current acting via the spin-transfer torque [10]. It is not present, however, when

Néel DWs move due to the spin Hall effect (SHE) generated when a current flows through an adjacent heavy-metal layer [11], but in this case the DWs are tilted towards the Bloch configuration as the current density increases, which reduces the efficiency of the SHE and leads to a saturation in the maximum velocity achievable. It is also absent in systems that exhibit antiferromagnetic coupling, such as antiferromagnets [12], ferrimagnets at angular-momentum compensation [13], and synthetic antiferromagnets [14], since DW tilting is virtually suppressed due to strong exchange coupling.

Alternative ways to move DWs in perpendicularly magnetized media that do not require external fields or charge currents are being explored. Some of them are based on using spatially variable physical quantities, such as the anisotropy [15–18] or temperature [19,20]. Others are based on geometry engineering and curvature effects [21]. Although the detailed mechanisms that drive the DWs in each case are different, all of them are based on the fact that the DW energy depends on a spatially variable quantity, and, consequently, a force appears that pushes a DW towards regions where its energy is lower. This force is typically dependent on the local gradient of the spatially variable quantity [17]; its effect is essentially equivalent to that of an external magnetic field, and, as such, WB occurs when the gradient exceeds a certain threshold value.

*mfa@usal.es

Recently, the effect of strain on the dynamics of magnetic DWs has been reported in several theoretical and experimental studies. It has been shown that, by optimizing the spatial profile of the strain, one can trigger magnetic DW motion along in-plane-magnetized strips [22–25]. Other work has shown that strain can be a useful tool to manipulate DW dynamics in perpendicularly magnetized films while they are driven by other means such as a magnetic field [26].

Here, we investigate the possibility of moving Néel DWs in perpendicularly magnetized media using an in-plane strain gradient. The main difference from the approaches mentioned above is that now not only the energy of a DW but also its equilibrium orientation depends on the in-plane strain. As will be shown, this leads to substantial changes in the DW dynamics with respect to the standard field-driven case. In particular, the interplay between the different torques involved keeps the internal DW angle bounded, preventing the appearance of precessional dynamics inside a DW for any arbitrary strain gradient.

The rest of the manuscript is organized as follows. The static properties of a DW in the presence of uniform strain are discussed in Sec. II. DW dynamics under strain gradients, which may be in-plane or perpendicular or both, is analyzed in Sec. III based on an extended one-dimensional model. Model predictions are tested by micromagnetic simulations under realistic conditions, as presented in Sec. IV. Finally, Sec. V presents the main conclusions and perspectives of the present work.

II. STATICS OF A DOMAIN WALL UNDER UNIFORM STRAIN

Before studying strain-induced DW dynamics, here we first analyze the effect of a uniform strain on the features of a DW at rest. To do so, we rely on both micromagnetic (μM) simulations and a reduced one-dimensional (1D) model. We consider a system that consists of a Néel DW located at the center of an infinite nanostrip subject to a uniform uniaxial strain ε_{ii} (where ii refers to the strain direction, $i : x, y, z$), as shown in Fig. 1(a). We assume that this ferromagnetic nanostrip is in contact with a heavy-metal layer not shown in the figure, and that the Néel configuration is favored over the Bloch one due to the interfacial Dzyaloshinskii-Moriya interaction (DMI) [11]. Within the 1D-model approach, the magnetization is assumed to change only along the longitudinal x axis [$\mathbf{M} = \mathbf{M}(x, t)$] [27–30], and the DW energy per unit area is given by

$$\sigma_{\text{DW}} = \int_{-\infty}^{+\infty} \left[A(\nabla \mathbf{m})^2 - K_u m_z^2 - \frac{\mu_0 M_s}{2} \mathbf{m} \cdot \mathbf{H}_d + D[m_z \nabla \mathbf{m} - (\mathbf{m} \cdot \nabla) m_z] + B_1 \varepsilon_{xx} m_x^2 + B_1 \varepsilon_{zz} m_z^2 \right] dx, \quad (1)$$

where $\mathbf{m}(x, t) = \mathbf{M}(x, t)/M_s$ is the normalized magnetization, \mathbf{H}_d is the self-magnetostatic field, and A, K_u, D , and B_1 are the exchange, anisotropy, DMI, and first magnetoelastic constants, respectively. We assume that the longitudinal in-plane strain ε_{xx} and the perpendicular strain ε_{zz} are the only components of the strain tensor present in the system and that $B_1 = -(3/2)\lambda_s(C_{11} - C_{12})$, with λ_s being the saturation magnetostriction and C_{11} and C_{12} the elastic constants [31]. We use the standard 1D ansatz for the DW profile [27,28,32], namely $\theta(x, t) = 2 \tan^{-1}[\exp((Q(x - q(t))/\Delta))]$, $\varphi(x, t) = \Phi(t)$, where $\theta(x, t)$ and $\varphi(x, t)$ are the spherical coordinates of the magnetization, as shown in Fig. 1, and q, Δ , and Φ are the DW position, width, and angle, respectively; the factor Q refers to an up-down ($Q = +1$) or down-up ($Q = -1$) DW configuration.

By integrating Eq. (1) using the 1D ansatz and assuming that the strain is uniform over the system, we obtain

$$\sigma_{\text{DW}} = \frac{2A}{\Delta} + 2\Delta(K_{\text{eff}} + K_{\text{sh}} \sin^2 \Phi + B_1 \varepsilon_{xx} \cos^2 \Phi - B_1 \varepsilon_{zz}) + \pi Q D \cos \Phi, \quad (2)$$

with $K_{\text{eff}} = K_u - \frac{1}{2}\mu_0 M_s^2$ and $K_{\text{sh}} = \frac{1}{2}\mu_0 M_s^2(N_y - N_x)$ being the effective and shape anisotropy constants, respectively. The internal DW angle at rest, Φ_0 , is obtained by minimizing Eq. (2) with respect to Φ . The resulting angle is

$$\Phi_0 = \cos^{-1} \left[\frac{\pi Q D}{4\Delta(K_{\text{sh}} - B_1 \varepsilon_{xx})} \right] \quad (3)$$

if $\pi|D| < 4\Delta|K_{\text{sh}} - B_1 \varepsilon_{xx}|$. Otherwise, $\Phi_0 = 0$ (π) for $D < 0$ (> 0). As the term proportional to ε_{zz} in Eq. (2) is independent of Φ , the equilibrium internal DW angle [Eq. (3)] is not affected by perpendicular strain. In contrast, Eq. (3) shows that the internal DW angle is dependent on the in-plane strain ε_{xx} . Figure 1(b) shows the equilibrium angle Φ_0 as a function of the in-plane strain for different values of D as computed from the 1D model (lines) and from micromagnetic simulations (dots). Typical material parameter values for Pt/Co are adopted for both the 1D model and the micromagnetic simulations, which are performed using the GPU-accelerated code MuMax3 [33]: $M_s = 0.58 \text{ MA m}^{-1}$, $A = 30 \text{ pJ m}^{-1}$, $K_u = 0.9 \text{ MJ m}^{-3}$, and $B_1 = 1.2 \text{ MJ m}^{-3}$ ($\lambda_s = -5 \times 10^{-5}$, $C_{11} = 298 \text{ GPa}$, and $C_{12} = 133 \text{ GPa}$). Bloch walls ($\Phi_0 = \pi/2$) are found in the absence of the DMI (for our nanowire dimensions, $N_y \ll N_x$, and, therefore, $K_{\text{sh}} < 0$), whereas a large DMI ($D = -1.8 \text{ mJ/m}^2$) stabilizes Néel DWs with right-handed chirality ($\Phi_0 = 0$). For intermediate values of the DMI, Fig. 1(b) shows that it is possible to tune the equilibrium angle sizably towards the Bloch (Néel) configuration by applying a moderate positive (negative) strain ($|\varepsilon_{xx}| < 5 \times 10^{-4}$). This effect is more visible in Fig. 1(c), where micromagnetic snapshots are shown for three different values of

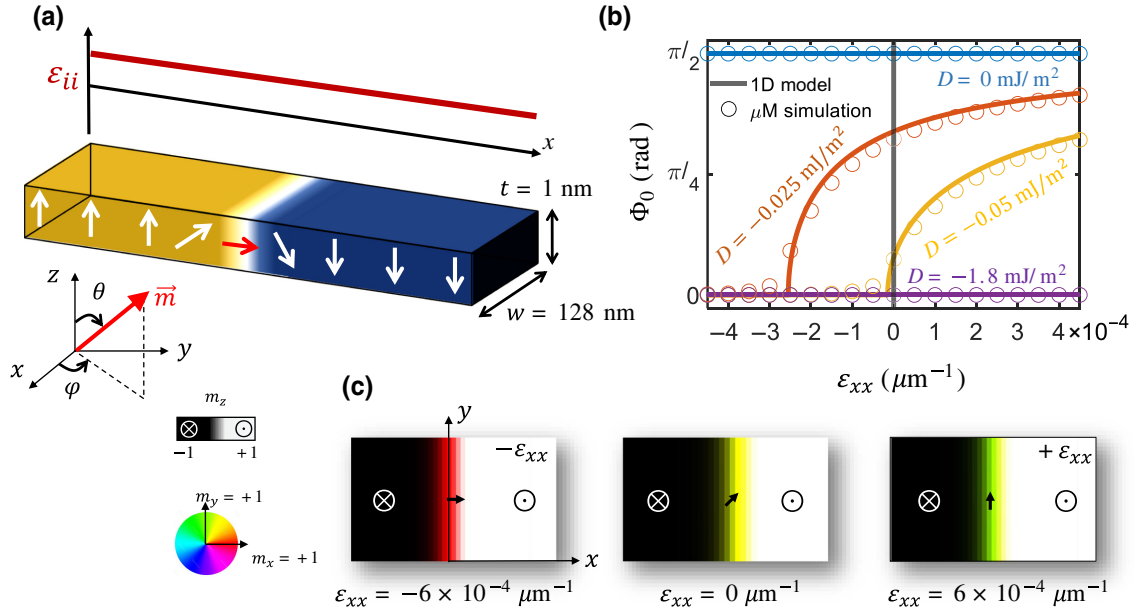


FIG. 1. (a) Schematic representation of the system under study. A Néel DW is located at the center of a ferromagnetic nanostrip subject to a uniform strain. (b) DW equilibrium angle Φ_0 as a function of the in-plane strain (ε_{xx}) for different values of the interface DMI constant D as computed from both micromagnetic simulations (dots) and the 1D model (lines). (c) Micromagnetic snapshots of down-up DW equilibrium patterns under different values of the in-plane strain (ε_{xx}) for a system with $D = -0.025$ mJ/m².

the in-plane strain (ε_{xx}). This is consistent with recent work [34] that showed how an in-plane anisotropy modulation can be used to transform between Bloch and Néel DWs. Indeed, our analysis shows that this can be done using in-plane strain. Namely, a tensile (compressive) strain favors Néel DWs for materials with $B_1 < 0$ (> 0). Besides, for a given material, changing the strain type (from tensile to compressive) can induce a transition from Bloch to Néel DWs under strains of realistic magnitudes. These results suggest that current-driven DW dynamics under spin-orbit torques could be also controlled with the assistance of a uniform in-plane strain [35].

III. STRAIN-INDUCED DOMAIN-WALL DYNAMICS

After proving the dependence of the equilibrium DW configuration on the in-plane strain, let us now focus on its dynamics in the presence of a space-dependent strain. To do so, we consider the same system as in Fig. 1(a) but with a DW subject to an in-plane uniaxial strain ε_{xx} that changes linearly along the longitudinal coordinate as shown in Fig. 2(a). To highlight the peculiarities of DW dynamics under such an in-plane strain, we compare it with the dynamics under a perpendicular strain ε_{zz} with the same linear profile [Fig. 2(a)] but with a positive slope since, as it will be shown later, the two gradients need to have opposite signs to produce DW motion in the same direction. We keep the same material parameters as in Sec.

II, along with a Gilbert damping constant $\alpha = 0.05$. To understand the strain-driven DW mechanism, we develop the one-dimensional model [27–29] by assuming that the strain varies linearly along the longitudinal x axis as

$$\varepsilon_{ii}(x) = \frac{\partial \varepsilon_{ii}}{\partial x} x = \varepsilon'_{ii} x. \quad (4)$$

After substituting Eq. (4) into Eq. (1) and integrating, the DW energy density now reduces to

$$\begin{aligned} \sigma_{\text{DW}} = & \frac{2A}{\Delta} + 2\Delta(K_{\text{eff}} + K_{\text{sh}} \sin^2 \Phi - B_1 \varepsilon'_{zz} q \\ & + B_1 \varepsilon'_{xx} q \cos^2 \Phi) + \pi Q D \cos \Phi, \end{aligned} \quad (5)$$

which indicates that the term proportional to ε'_{zz} does not depend on the DW angle Φ , whereas the term proportional to ε'_{xx} does. Using Eq. (5), equations describing the DW dynamics within the 1D approach can be obtained following a conventional procedure [36], which is detailed in the Supplemental Material [37], yielding

$$(1 + \alpha^2) \frac{\dot{q}}{\Delta} = -\alpha \Gamma_A(\Phi) + Q \Gamma_B(q, \Phi), \quad (6a)$$

$$(1 + \alpha^2) \dot{\Phi} = -Q \Gamma_A(\Phi) - \alpha \Gamma_B(q, \Phi), \quad (6b)$$

where

$$\Gamma_A(\Phi) = \gamma_0 \Delta H_{\text{mel}} (\varepsilon'_{xx} \cos^2 \Phi - \varepsilon'_{zz}), \quad (7a)$$

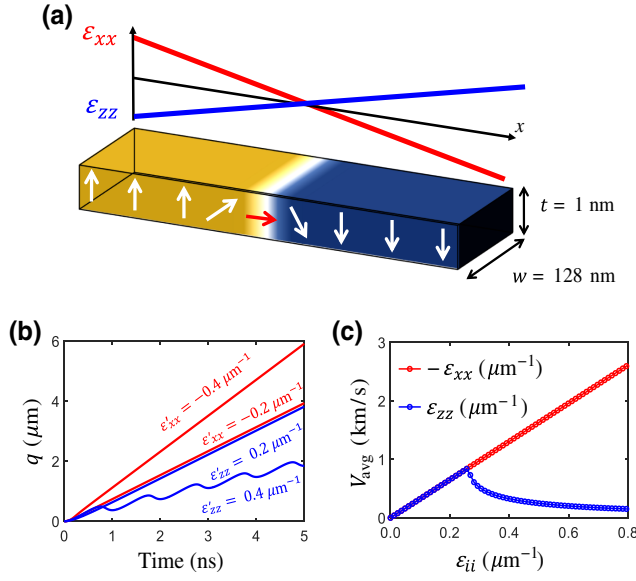


FIG. 2. (a) Schematic representation of the system under study. A Néel DW is initially located at the center of a ferromagnetic nanostrip subject to a strain gradient. The in-plane and perpendicular strain profiles are shown by red and blue colors, respectively. (b) DW position (q) versus time when driven by two different in-plane (red) and perpendicular (blue) strain gradients. (c) Average DW velocity versus strain slope for the in-plane (red) and perpendicular (blue) cases.

$$\Gamma_B(\Phi, q) = \gamma_0 \left[\left(\frac{H_{\text{sh}}}{2} - H_{\text{mel}} \varepsilon'_{xx} q \right) \sin 2\Phi - \frac{\pi}{2} Q H_{\text{DMI}} \sin \Phi \right], \quad (7b)$$

and where $H_{\text{mel}} = B_1/\mu_0 M_s$, $H_{\text{sh}} = 2K_{\text{sh}}/\mu_0 M_s$, and $H_D = D/\mu_0 M_s \Delta$ are the magnetoelastic, shape anisotropy, and DMI fields, respectively. In what follows, we refer to the case of an in-plane strain gradient when $\varepsilon'_{xx} \neq 0$ and $\varepsilon'_{zz} = 0$, and to the case of a perpendicular strain gradient when $\varepsilon'_{xx} = 0$ and $\varepsilon'_{zz} \neq 0$.

In analogy with the conventional field-driven case [28, 38], the term $-\alpha\Gamma_A$ in Eq. (6a) can be considered as the driving agent that pushes the DW along the direction of decreasing energy, i.e., increasing tensile (compressive) strain if $B_1 < 0$ (> 0) for the in-plane-strain-gradient case and increasing compressive (tensile) strain if $B_1 < 0$ (> 0) for the perpendicular case. On the other hand, the two terms on the rhs of Eq. (6b) can be viewed as the precessional ($-Q\Gamma_A$) and damping ($-\alpha\Gamma_B$) in-plane torques that govern the internal DW-angle dynamics. Two main differences can be readily noticed between the in-plane and perpendicular cases. First, the contribution of ε'_{xx} to the precessional torque ($-Q\Gamma_A$) is modulated by a factor $\cos^2 \Phi$, which is not the case for ε'_{zz} . Second, ε'_{xx} contributes to the damping torque ($-\alpha\Gamma_B$), whereas ε'_{zz} does

not. Moreover, this contribution also depends on the DW position q [see Eq. (7b)]. As we show below, this term has a strong impact on the response of the DW to an in-plane strain gradient.

Figure 2(b) shows the time evolution of the DW position q predicted from the 1D model for two representative values of in-plane (red) and perpendicular (blue) strain gradients. Note that the dependences of the DW energy on ε'_{xx} and ε'_{zz} are of opposite sign [see Eq. (5)], and, therefore, to produce DW motion along the same direction, the signs of the gradient also need to be opposite. In our case $B_1 > 0$, so $\varepsilon'_{xx} < 0$ and $\varepsilon'_{zz} > 0$ lead to DW motion along the positive direction ($+x$). As can be observed in Fig. 2(b), for small strain gradients ($|\varepsilon'_{ii}| = 0.2 \mu\text{m}^{-1}$), steady DW motion with similar velocities is achieved in both the in-plane and the perpendicular case. However, if the strain gradient is increased ($|\varepsilon'_{ii}| = 0.4 \mu\text{m}^{-1}$), the response is very different. For a perpendicular strain ($|\varepsilon'_{zz}| = 0.4 \mu\text{m}^{-1}$), the DW displays turbulent motion with a low average velocity, which is typical of when the system exceeds the WB limit. In contrast, the DW moves steadily with a higher velocity in the in-plane case ($|\varepsilon'_{xx}| = 0.4 \mu\text{m}^{-1}$). Figure 2(c) shows the DW velocity averaged over a temporal window of 5 ns as a function of the strain gradient for both the in-plane (red) and the perpendicular (blue) case. For a perpendicular strain, we observe WB at $\varepsilon'_{zz, \text{WB}} = \alpha\pi H_{\text{DMI}}/2H_{\text{mel}}\Delta \approx 0.26 \mu\text{m}^{-1}$ as one would expect, considering that the effect of a perpendicular strain gradient is equivalent to that of an external magnetic field $H_{\text{eq}} = H_{\text{mel}}\varepsilon'_{zz}\Delta$. Below the WB limit, the DW moves rigidly and reaches a terminal velocity proportional to the strain gradient [$V = (\gamma_0\Delta^2/\alpha)H_{\text{mel}}\varepsilon'_{zz}$], whereas above it the DW undergoes continuous internal precession, the velocity is no longer uniform, and the DW mobility is significantly reduced. For the in-plane case, however, no WB is observed, and the DW mobility remains constant for arbitrarily high values of the strain gradient. This absence of WB in DW motion driven by an in-plane strain gradient is the main result of our work, and, in what follows, we focus on explaining the mechanism that makes it possible.

Figure 3(a) shows the time evolution of the DW angle Φ (top) and its instantaneous velocity V_{inst} (bottom) for different values of the in-plane strain gradient ε'_{xx} . As can be observed, a transient period where both Φ and V_{inst} change nonmonotonically occurs before the DW asymptotically reaches a steady velocity, and the angle goes back towards its initial value ($\Phi = 0$). In order to shed light on this process, we analyze the different in-plane torques that govern the dynamics of the DW angle in Eq. (6b). On the one hand, we have the precessional component of the driving force, $-Q\Gamma_A$, which drives the angle away from its equilibrium orientation. On the other hand, the damping torque ($-\alpha\Gamma_B$) has three contributions, i.e., $\alpha\Gamma_{\text{sh}} = -\alpha\gamma_0(H_{\text{sh}}/2)\sin 2\Phi$, $\alpha\Gamma_{\text{DMI}} = \alpha\gamma_0(Q\pi H_{\text{DMI}}/2)\sin \Phi$, and $\alpha\Gamma_{\varepsilon'_{xx}}(q) = \alpha\gamma_0 H_{\text{mel}}\varepsilon'_{xx}q \sin 2\Phi$.

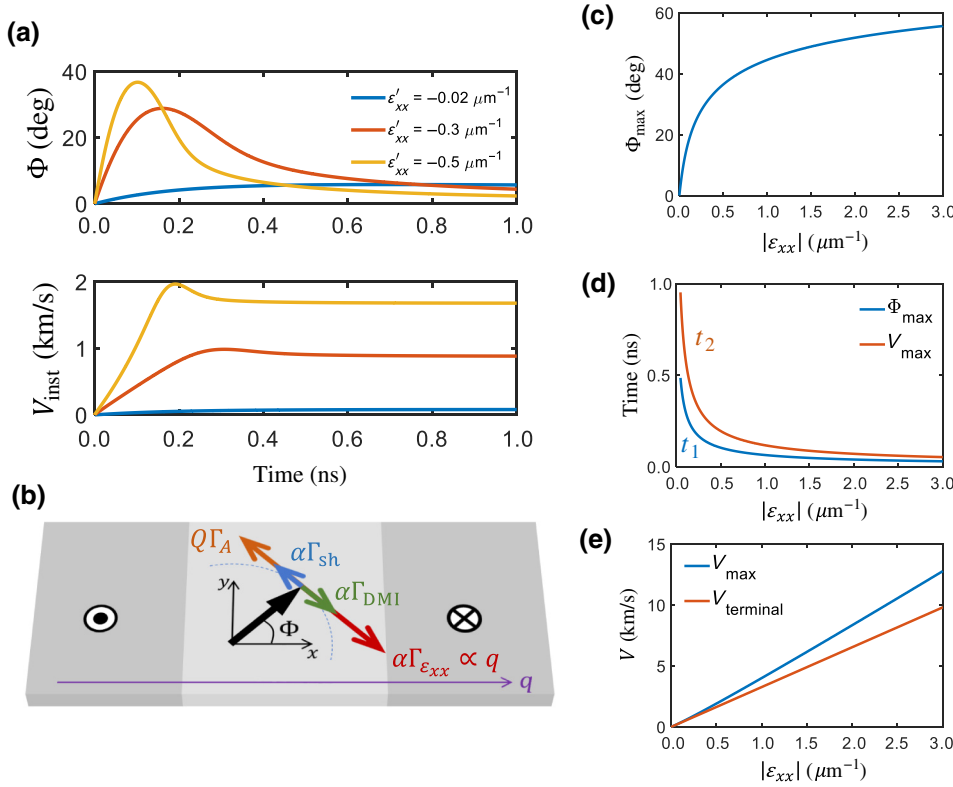


FIG. 3. (a) Temporal evolution of the DW angle and instantaneous velocity when driven by an in-plane strain gradient ($\varepsilon'_{xx} \neq 0$ and $\varepsilon'_{zz} = 0$). (b) Schematic representation of the different torque contributions to the DW dynamics studied. (c) Maximum tilting of the DW angle versus strain gradient. (d) Characteristic time needed to reach the maximum angle (blue) and maximum velocity (orange). (e) Maximum (blue) and terminal (orange) velocities versus strain gradient.

The first two of these are the standard shape-anisotropy and DMI in-plane damping torques and are always present, regardless of the nature of the force that moves the DW. The third contribution, $\alpha\Gamma_{\varepsilon'_{xx}}(q)$, is specific to the case of an in-plane strain gradient, and, unlike the situation for the other contributions, its strength depends explicitly on the DW position q . These four in-plane torques are schematically represented in Fig. 3(b), where their signs are consistent with an up-down right-handed ($Q = +1$) DW moving along the $x > 0$ direction.

As soon as the DW starts moving due to the driving torque $-\alpha\Gamma_A$, the corresponding precessional component $-Q\Gamma_A$ tilts its angle away from the equilibrium orientation, and a restoring torque appears, trying to bring it back to its orientation at rest. When the driving force is an external field or a perpendicular strain gradient, the total restoring torque is given by $\alpha\Gamma_{\text{sh}} + \alpha\Gamma_{\text{DMI}}$, and if the driving force exceeds a certain threshold value, such a restoring torque cannot balance the precessional torque, and WB takes place. However, for an in-plane strain gradient the third term, $\alpha\Gamma_{\varepsilon'_{xx}}(q)$, which opposes the precessional torque, also comes into play, with the peculiarity that its strength increases as the DW moves along the strain gradient [Fig. 3(b)], therefore contributing to bringing the angle closer to its value at rest. In fact, this term guarantees that the DW angle remains bounded during motion regardless of the magnitude of the driving force, since its strength, like that of the precessional torque, is proportional to the strain gradient ε'_{xx} [Eq. (7b)].

With this idea in mind, the transient behavior observed in Fig. 3(a) can be understood as follows. As the DW starts moving and the angle deviates from its equilibrium value, the strength of the in-plane precessional torque $-Q\Gamma_A$ decreases, whereas the in-plane damping torque $-\alpha\Gamma_B$ increases. Since they have opposite signs, the total in-plane torque is gradually reduced, up to a point where the two terms balance out ($Q\Gamma_A + \alpha\Gamma_B = 0$) and the tilting angle reaches its maximum deviation (Φ_{max}). As shown in Fig. 3(c), this maximum deviation Φ_{max} increases with the strain gradient ε'_{xx} but saturates around $\pi/3$, proving our finding that the angle remains bounded no matter how large the strain gradient is. After Φ_{max} is reached at a certain time t_1 , the total in-plane torque changes sign ($|\alpha\Gamma_B| > |Q\Gamma_A|$) and Φ starts decreasing, whereas the DW velocity continues increasing, up to a point where it reaches its maximum value V_{max} at a later time t_2 . Figure 3(d) shows how the two characteristic times of this transient dynamics, t_1 and t_2 , depend on the strain gradient. As can be observed, they decrease in a similar fashion. As the DW moves further into the region of increasing strain, the term $\alpha\Gamma_{\varepsilon'_{xx}}$ becomes dominant ($|\Gamma_{\varepsilon'_{xx}}| \gg |\Gamma_{\text{DMI}}|, |\Gamma_{\text{sh}}|$), and the DW angle gradually goes back to its initial Néel orientation according to $\Phi(q) = \tan^{-1}(Q\Delta/2\alpha q)$. The DW velocity, meanwhile, asymptotically reaches a terminal value given by

$$V_{\text{term}} = \frac{\gamma_0 H_{\text{mel}} \Delta^2}{\alpha} \varepsilon'_{xx}. \quad (8)$$

Figure 3(e) shows both the terminal and the maximum velocity as a function of the in-plane strain gradient. While the first velocity displays a perfectly linear trend, the second has a slightly stronger dependence, so that the difference between them increases with ε'_{xx} .

Up to here, we have investigated DW motion in the presence of separate in-plane and perpendicular strain gradients. Although this assumption could be applied to some piezoelectric/magnetic systems, depending on the cut direction of the piezoelectric substrate, it is also possible to find that both in-plane and perpendicular strains are present in the system [39]. Therefore, investigating their joint effect on DW motion is also timely. Thus, we consider the system in Fig. 2(a) with both $\varepsilon'_{xx} \neq 0$ and $\varepsilon'_{zz} \neq 0$. We parameterize these as $\varepsilon'_{zz} = -\beta\varepsilon'_{xx}$, with $\beta = |\varepsilon'_{zz}/\varepsilon'_{xx}|$ being the ratio between them. Considering that they need to have opposite signs to produce DW motion in the same direction, the expression in Eq. (7a) becomes $\Gamma_A(\Phi) = \gamma_0\Delta H_{\text{mel}}\varepsilon'_{xx}(\cos^2\Phi + \beta)$, whereas $\Gamma_B(\Phi, q)$ remains the same as in Eq. (7b).

Figure 4 shows the dynamics of DWs for different values of the ratio β . As can be noticed from Fig. 4(a), where the average DW velocity is plotted versus the strain gradient, the system does not show any WB for any value of β . However, when we look at the instantaneous velocity plotted in Fig. 4(b) for a relatively high strain gradient ($\varepsilon'_{xx} = -0.61 \mu\text{m}^{-1}$), two regimes are depicted. On the one hand, when $\beta < 1$ the system behaves similarly to the pure in-plane-strain-gradient case described earlier, where no instabilities are found. On the other hand, when $\beta \geq 1$, the instantaneous DW velocity exhibits nonlinear behavior

during the transient dynamics. After reaching a maximum, the DW velocity decreases towards its terminal value. To shed more light on this complex transient dynamics, Fig. 4(c) shows the longitudinal component of the internal DW magnetization $m_x = \cos\Phi$ as a function of time for different values of β . It can be seen from Fig. 4(c) that the internal DW magnetization oscillates during a transient period for $\beta \geq 1$, leading to the onset of turbulent motion. Afterwards, it reaches an equilibrium value, and the DW recovers steady motion. We note that the behavior shown in Fig. 4 depends on both β and ε'_{xx} , and, therefore, for values of ε'_{xx} larger than the ones shown here, the transient period of unstable DW motion appears for $\beta < 1$ as well.

We can interpret the results in Fig. 4 similarly to those obtained for in-plane strain gradients in terms of the action of the torques involved. When the contribution of ε'_{zz} is added, the strength of the precession torque $-Q\Gamma_A$ increases, while the damping torque $-\alpha\Gamma_B$ remains unaffected. This leads to a local breakdown of the compensation scheme described earlier, and consequently turbulent motion can take place if ε'_{zz} is large enough. On the other hand, as the DW moves, the damping torque $-\alpha\Gamma_B \propto q$ gains in strength, and eventually is able to compensate the precession torque $-Q\Gamma_A$. Then, the DW angle goes back towards its equilibrium configuration ($\Phi = 0$), and the DW recovers steady motion with a constant terminal velocity given by

$$V_{\text{term}} = \frac{\gamma_0 H_{\text{mel}} \Delta^2}{\alpha} \varepsilon'_{xx} (1 + \beta), \quad (9)$$

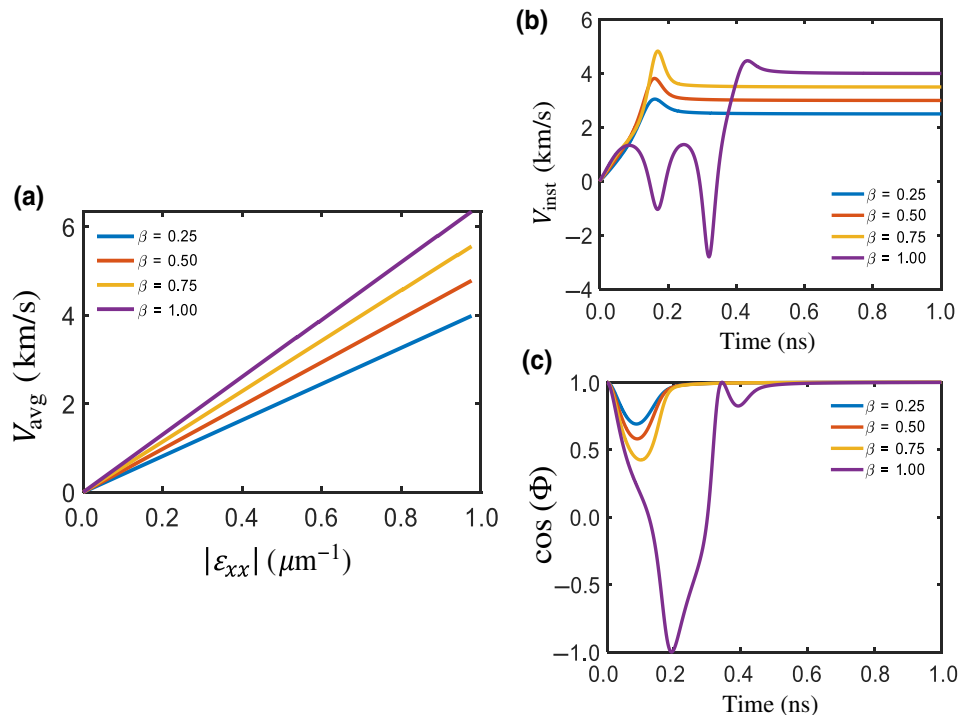


FIG. 4. (a) Average DW velocity as a function of the strain gradient for different values of $\beta = |\varepsilon'_{zz}/\varepsilon'_{xx}|$. (b) Instantaneous DW velocity as a function of time for different values of β and $\varepsilon'_{xx} = -0.61 \mu\text{m}^{-1}$. (c) DW position as a function of time for different values of β and $\varepsilon'_{xx} = -0.61 \mu\text{m}^{-1}$. (d) Time evolution of the longitudinal component of the internal DW magnetization ($m_x = \cos\Phi$) for different ratios β and $\varepsilon'_{xx} = -0.61 \mu\text{m}^{-1}$.

which shows that adding the contribution of the perpendicular strain gradient enhances significantly the DW motion in the steady regime.

IV. MICROMAGNETIC SIMULATIONS

In the previous section, we show theoretically the absence of WB for DWs driven by in-plane strain gradients based on the 1D model. In doing so, we explore high-strain situations to prove that steady DW dynamics can be reached regardless of the strength of the driving force. However, in practice there are limitations on the magnitude of the strain gradient that can be applied and the distance over which it can be maintained. Not only can a large strain gradient induce mechanical damage in the device but also, if the strain is large enough to compete with the perpendicular anisotropy ($|B_1 \varepsilon_{xx}| \sim K_{\text{eff}}$), which in our case happens when $\varepsilon_{xx} \sim 0.06$, the nucleation of in-plane domains can start to take place, and the system depicted in Fig. 2(a), with a DW separating two antiparallel domains, may no longer be stable. Therefore, to explore the plausibility of our proposal under realistic conditions, micromagnetic simulations are performed using the same

material parameters as given before and a strain gradient over the strip length, which is fixed at $1 \mu\text{m}$. Figure 5(a) shows the time evolution of the DW angle Φ for different values of ε'_{xx} as computed from both the micromagnetic simulations (dots) and the 1D model (lines). It can be observed that the simulations support the 1D results shown in Fig. 3. Indeed, the internal angle remains bounded even for the highest values of the strain gradient. To get good agreement between the 1D model and the μM results, it is necessary to take into account in the former the sizable variations of the width of the DW [9] as it goes deeper into the highly strained region, and its effect on the demagnetizing factors [40]. Using the same method as for the (q, Φ) 1D dynamic equations [29,36], the following additional dynamic equation for the DW width is obtained:

$$\dot{\Delta} = \frac{12\gamma_0}{\alpha\mu_0 M_s \pi^2} \left[\frac{A}{\Delta} - \Delta (K_{\text{eff}} + K_{\text{sh}} \sin^2 \Phi - B_1 \varepsilon'_{zz} q + B_1 \varepsilon'_{xx} q \cos^2 \Phi) \right]. \quad (10)$$

Figure 5(b) shows the average DW velocity V_{avg} as a function of the in-plane strain gradient for different values of α , obtained from the micromagnetic simulations

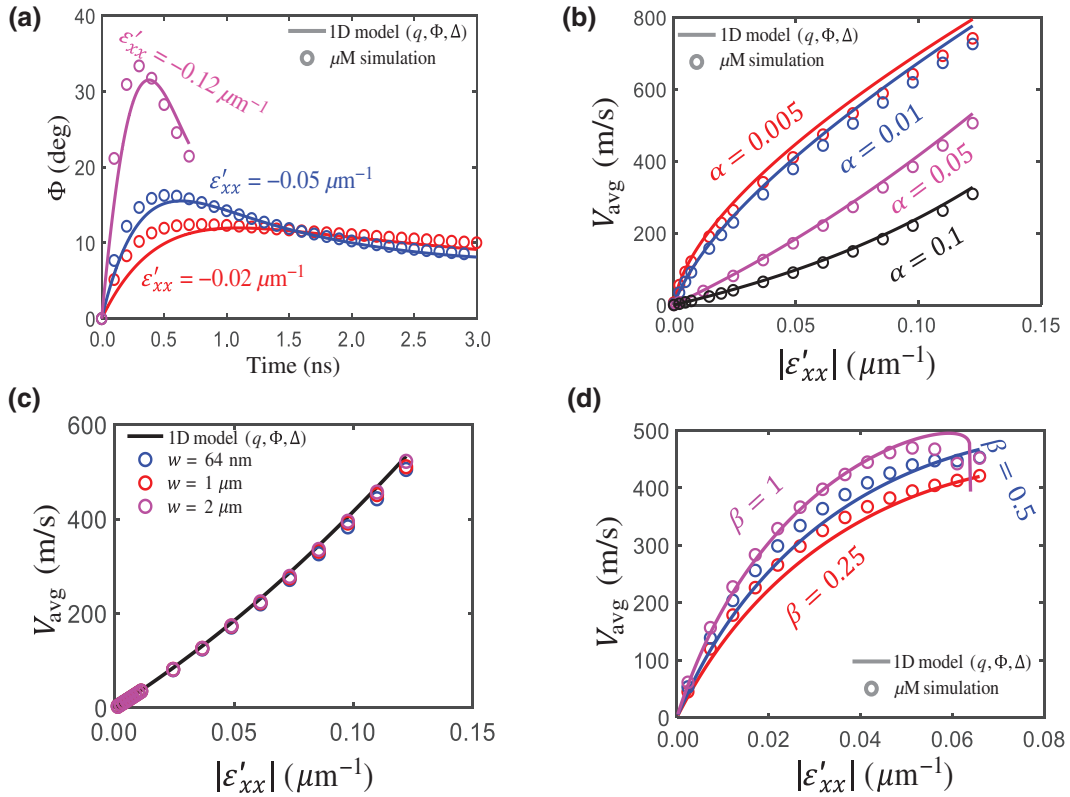


FIG. 5. (a) Time evolution of the DW angle Φ for different values of the in-plane strain gradient (ε'_{xx}). (b) Average DW velocity as a function of ε'_{xx} for different values of the damping constant α . (c) Average DW velocity for different strip widths under in-plane strain gradients and $\alpha = 0.05$. (d) Average DW velocity as a function of the strain gradient for different values of the ratio between the perpendicular and in-plane strain gradients $\beta = |\varepsilon'_{zz}/\varepsilon'_{xx}|$. In all graphs, the micromagnetic results and the 1D results are shown by dots and lines, respectively.

(dots) and from the 1D model (lines). Because of the limitations mentioned earlier, the terminal velocity predicted by the 1D model [Eq. (8)] is not accessible in a $1\text{-}\mu\text{m}$ -long strip. On the other hand, the nonlinear dependence on ε'_{xx} observed for all values of α is due to the fact that the velocity is averaged over a short time interval in which the DW velocity is highly nonuniform, unlike the case in Fig. 1(c), where the time interval (5 ns) is significantly larger than this transient period, so that $V_{\text{avg}} \approx V_{\text{term}}$. In any case, Fig. 5(b) confirms that the absence of WB revealed by our 1D model remains true under realistic modeling. In Fig. 5(c), we show the average DW velocity versus the strain gradient for different widths of the ferromagnetic strip. As can be seen, the average velocity is not affected by the strip width, and good agreement with the 1D model is found. This confirms that the physics underlying DW motion under strain demonstrated by the 1D model is valid not only for narrow strips, but also for wide ones.

Figure 5(d) shows the average DW velocity in the case where in-plane and perpendicular strain gradients are applied simultaneously to the system, with a ratio $\beta = |\varepsilon'_{zz}/\varepsilon'_{xx}|$. As can be observed, the micromagnetic simulations confirm the onset of turbulent DW motion at $\varepsilon'_{xx} = -0.077\ \mu\text{m}^{-1}$ if the two strain gradients are of the same magnitude ($\beta = 1$). However, the additional contribution of ε'_{zz} increases the average DW velocity. The dynamics after the transient period described in Sec. III for the 1D model (where the DW recovers steady motion) is not accessible via micromagnetic simulations, because of the limitations on the strain magnitude explained above.

To sum up, our simulations show that high DW velocities can be achieved under realistic conditions, especially if we take into account that, as shown in our previous publications [41,42], in-plane strain gradients in the order of $10^{-2}\ \mu\text{m}^{-1}$ can be realized in hybrid ferromagnetic/piezoelectric devices by applying moderate voltages between conveniently located electrodes on the piezoelectric substrate.

V. CONCLUSION

We study the influence of strain on the statics and dynamics of DWs in a ferromagnetic strip with perpendicular anisotropy. Our theoretical study shows that a uniform strain can be used to tune the internal DW angle between the Bloch and Néel configurations. It is also shown that DW dynamics driven by an in-plane strain gradient is qualitatively different from the response to other driving forces, such as an external field, a spin-polarized current, or a perpendicular strain gradient. In particular, such dynamics occurs without Walker breakdown, and, ideally, a DW velocity proportional to the strain gradient is obtained regardless of the magnitude of the strain gradient. We show that the origin of this phenomenon lies in the fact that the internal DW angle in equilibrium depends on the

strain. This leads to a dynamic torque that opposes tilting of the internal DW angle and whose strength increases as the DW moves towards increasingly strained regions, and this torque prevents the onset of internal DW oscillations. On the other hand, the maximum DW velocity achievable with our approach is limited not by the intrinsic dynamic properties of DWs but by the feasibility of keeping perpendicularly magnetized domains stable in regions of high in-plane strain. In any case, our micromagnetic simulations show that average velocities in the order of 500 m/s can be achieved under realistic conditions easily achievable in experimental setups. These velocities are in the range of spin-orbit-torque-driven DW motion but are reached with much less energy dissipation, since Joule heating is absent. Furthermore, our system reveals complex dynamics where the DW angle and, therefore, also the inertia of the DW are not uniquely determined by its velocity but can be tuned by a large amount by means of strain, which opens up a new avenue to explore dynamic phenomena.

ACKNOWLEDGMENTS

We gratefully acknowledge financial support from the European Union H2020 Program under MSCA MagnEFi ITN Grant No. 860060, from the Ministerio de Educación y Ciencia through the project MAT2017-87072-C4-1-P, from the Ministerio de Ciencia e Innovación under the project PID2020-117024GB-C41, and from the Consejería de Educación of Castilla y León under the projects SA114P20 and SA299P18.

- [1] S. Parkin and S. H. Yang, Memory on the racetrack, *Nat. Nanotechnol.* **10**, 195 (2015).
- [2] X. Zhang, N. Vernier, Z. Cao, Q. Leng, A. Cao, D. Ravelosona, and W. Zhao, Magnetoresistive sensors based on the elasticity of domain walls, *Nanotechnology* **29**, 365502 (2018).
- [3] J. H. Franken, H. J. Swagten, and B. Koopmans, Shift registers based on magnetic domain wall ratchets with perpendicular anisotropy, *Nat. Nanotechnol.* **7**, 499 (2012).
- [4] Z. Luo, A. Hrabec, T. P. Dao, G. Sala, S. Finizio, J. Feng, S. Mayr, J. Raabe, P. Gambardella, and L. J. Heyderman, Current-driven magnetic domain-wall logic, *Nature* **579**, 214 (2020).
- [5] M. Alamdar, T. Leonard, C. Cui, B. P. Rimal, L. Xue, O. G. Akinola, T. P. Xiao, J. S. Friedman, C. H. Bennett, M. J. Marinella, and J. A. C. Incorvia, Domain wall-magnetic tunnel junction spin-orbit torque devices and circuits for in-memory computing, *Appl. Phys. Lett.* **118**, 112401 (2021).
- [6] K. Yue, Y. Liu, R. K. Lake, and A. C. Parker, A brain-plausible neuromorphic on-the-fly learning system implemented with magnetic domain wall analog memristors, *Sci. Adv.* **5**, 8170 (2019).
- [7] A. Hubert and R. Schäfer, *Magnetic Domains: The Analysis of Magnetic Microstructures* (Springer Science & Business Media, Heiderberg, 2008).

- [8] S. Glathe, R. Mattheis, and D. V. Berkov, Direct observation and control of the Walker breakdown process during a field driven domain wall motion, *Appl. Phys. Lett.* **93**, 072508 (2008).
- [9] A. Mougin, M. Cormier, J. P. Adam, P. J. Metaxas, and J. Ferré, Domain wall mobility, stability and Walker breakdown in magnetic nanowires, *EPL* **78**, 57007 (2007).
- [10] K. S. Ryu, L. Thomas, S. H. Yang, and S. Parkin, Chiral spin torque at magnetic domain walls, *Nat. Nanotechnol.* **8**, 527 (2013).
- [11] E. Martinez, S. Emori, and G. S. Beach, Current-driven domain wall motion along high perpendicular anisotropy multilayers: The role of the Rashba field, the spin Hall effect, and the Dzyaloshinskii-Moriya interaction, *Appl. Phys. Lett.* **103**, 072406 (2013).
- [12] T. Shiino, S. H. Oh, P. M. Haney, S. W. Lee, G. Go, B. G. Park, and K. J. Lee, Antiferromagnetic Domain Wall Motion Driven by Spin-Orbit Torques, *Phys. Rev. Lett.* **117**, 087203 (2016).
- [13] S. A. Siddiqui, J. Han, J. T. Finley, C. A. Ross, and L. Liu, Current-Induced Domain Wall Motion in a Compensated Ferrimagnet, *Phys. Rev. Lett.* **121**, 057701 (2018).
- [14] S. H. Yang, K. S. Ryu, and S. Parkin, Domain-wall velocities of up to 750 m s^{-1} driven by exchange-coupling torque in synthetic antiferromagnets, *Nat. Nanotechnol.* **10**, 221 (2015).
- [15] W. H. Li, Z. Jin, D. L. Wen, X. M. Zhang, M. H. Qin, and J. M. Liu, Ultrafast domain wall motion in ferrimagnets induced by magnetic anisotropy gradient, *Phys. Rev. B* **101**, 024414 (2020).
- [16] L. Sanchez-Tejerina, O. Alejos, V. Raposo, and E. Martinez, Current-driven domain wall motion along ferromagnetic strips with periodically-modulated perpendicular anisotropy, *J. Appl. Phys.* **123**, 223904 (2018).
- [17] D. L. Wen, Z. Y. Chen, W. H. Li, M. H. Qin, D. Y. Chen, Z. Fan, M. Zeng, X. B. Lu, X. S. Gao, and J. M. Liu, Ultralow-loss domain wall motion driven by a magnetocrystalline anisotropy gradient in an antiferromagnetic nanowire, *Phys. Rev. Res.* **2**, 013166 (2020).
- [18] J. H. Franken, M. Hoeijmakers, R. Lavrijsen, and H. J. Swagten, Domain-wall pinning by local control of anisotropy in Pt/Co/Pt strips, *J. Phys. Condens. Matter* **24**, 024216 (2012).
- [19] X. S. Wang and X. R. Wang, Thermodynamic theory for thermal-gradient-driven domain-wall motion, *Phys. Rev. B* **90**, 014414 (2014).
- [20] F. Schlickeiser, U. Ritzmann, D. Hinzke, and U. Nowak, Role of Entropy in Domain Wall Motion in Thermal Gradients, *Phys. Rev. Lett.* **113**, 097201 (2014).
- [21] K. V. Yershov, V. P. Kravchuk, D. D. Sheka, O. V. Pylypovskiy, D. Makarov, and Y. Gaididei, Geometry-induced motion of magnetic domain walls in curved nanostripes, *Phys. Rev. B* **98**, 060409 (2018).
- [22] M. T. Bryan, J. Dean, and D. A. Allwood, Dynamics of stress-induced domain wall motion, *Phys. Rev. B* **85**, 144411 (2012).
- [23] Z. Xiao, R. Lo Conte, C. Chen, C.-Y. Liang, A. Sepulveda, J. Bokor, G. P. Carman, and R. N. Candler, Bi-directional coupling in strain-mediated multiferroic heterostructures with magnetic domains and domain wall motion, *Sci. Rep.* **8**, 5207 (2018).
- [24] G. Yu, S. Shi, R. Peng, R. Guo, Y. Qiu, G. Wu, Y. Li, M. Zhu, and H. Zhou, Strain-driven magnetic domain wall dynamics controlled by voltage in multiferroic heterostructures, *J. Magn. Magn. Mater.* **552**, 169229 (2022).
- [25] F. Chen, X. Ge, W. Luo, R. Xing, S. Liang, X. Yang, L. You, R. Xiong, Y. Otani, and Y. Zhang, Strain-Induced Megahertz Oscillation and Stable Velocity of an Antiferromagnetic Domain Wall, *Phys. Rev. Appl.* **15**, 014030 (2021).
- [26] P. Shepley, A. Rushforth, M. Wang, G. Burnell, and T. Moore, Modification of perpendicular magnetic anisotropy and domain wall velocity in Pt/Co/Pt by voltage-induced strain, *Sci. Rep.* **5**, 1 (2015).
- [27] N. L. Schryer and L. R. Walker, The motion of 180 domain walls in uniform dc magnetic fields, *J. Appl. Phys.* **45**, 5406 (1974).
- [28] A. Thiaville, S. Rohart, É. Jué, V. Cros, and A. Fert, Dynamics of Dzyaloshinskii domain walls in ultrathin magnetic films, *EPL (Europhysics Letters)* **100**, 57002 (2012).
- [29] O. Alejos, V. Raposo, and E. Martinez, in *Materials Science and Technology* (John Wiley and Sons, Ltd, 2020), Chap. 5, p. 1.
- [30] A. Malozemoff and J. Slonczewski, in *Magnetic Domain Walls in Bubble Materials*, edited by A. Malozemoff and J. Slonczewski (Academic Press, New York, 1979), p. 77.
- [31] C.-Y. Liang, S. M. Keller, A. E. Sepulveda, A. Bur, W.-Y. Sun, K. Wetzlar, and G. P. Carman, Modeling of magnetoelastic nanostructures with a fully coupled mechanical-micromagnetic model, *Nanotechnology* **25**, 435701 (2014).
- [32] A. Malozemoff and J. Slonczewski, *Magnetic Domain Walls in Bubble Materials*, *Appl. Solid State Sci.* (Academic Press, New York, NY, 1979).
- [33] A. Vansteenkiste, J. Leliaert, M. Dvornik, M. Helsen, F. Garcia-Sanchez, and B. Van Waeyenberge, The design and verification of MuMax3, *AIP. Adv.* **4**, 107133 (2014).
- [34] K. J. A. Franke, C. Ophus, A. K. Schmid, and C. H. Marrows, Switching between Magnetic Bloch and Néel Domain Walls with Anisotropy Modulations, *Phys. Rev. Lett.* **127**, 127203 (2021).
- [35] S. Emori, U. Bauer, S. Ahn, E. Martinez, and G. Beach, Current-driven dynamics of chiral ferromagnetic domain walls, *Nat. Mater.* **12**, 611 (2013).
- [36] A. Malozemoff and J. Slonczewski, in *Magnetic Domain Walls in Bubble Materials*, edited by A. Malozemoff and J. Slonczewski (Academic Press, New York, 1979), p. 123.
- [37] See Supplemental Material at <http://link.aps.org/supplemental/10.1103/PhysRevApplied.18.044023> for more details about the derivation of the analytical model.
- [38] P. J. Metaxas, J. P. Jamet, A. Mougin, M. Cormier, J. Ferré, V. Baltz, B. Rodmacq, B. Dieny, and R. L. Stamps, Creep and Flow Regimes of Magnetic Domain-Wall Motion in Ultrathin Pt/Co/Pt Films with Perpendicular Anisotropy, *Phys. Rev. Lett.* **99**, 217208 (2007).
- [39] P. Han, W. Yan, J. Tian, X. Huang, and H. Pan, Cut directions for the optimization of piezoelectric coefficients of lead magnesium niobate lead titanate ferroelectric crystals, *Appl. Phys. Lett.* **86**, 052902 (2005).

- [40] A. Skaugen, P. Murray, and L. Laurson, Analytical computation of the demagnetizing energy of thin-film domain walls, *Phys. Rev. B* **100**, 094440 (2019).
- [41] R. Yanes, F. Garcia-Sanchez, R. F. Luis, E. Martinez, V. Raposo, L. Torres, and L. Lopez-Diaz, Skyrmion motion induced by voltage-controlled in-plane strain gradients, *Appl. Phys. Lett.* **115**, 132401 (2019).
- [42] M. Fattouhi, F. García-Sánchez, R. Yanes, V. Raposo, E. Martínez, and L. Lopez-Diaz, Electric Field Control of the Skyrmion Hall Effect in Piezoelectric-Magnetic Devices, *Phys. Rev. Appl.* **16**, 044035 (2021).